# Efficient photocatalytic hydrogen evolution on N-deficient g-C$_3$N$_4$ achieved by a molten salt post-treatment approach

Junying Liu, Wenjian Fang, Zhidong Wei, Zhen Qin, Zhi Jiang, Wenfeng Shangguan[*]

*Research Center for Combustion and Environment Technology, Shanghai Jiao Tong University, 800 Dong Chuan Road, Shanghai 200240, China*

## ARTICLE INFO

## ABSTRACT

Graphitic carbon nitride (g-C$_3$N$_4$) is a fascinating metal-free photocatalyst for active solar hydrogen production. However, the photocatalytic activity of pristine g-C$_3$N$_4$ is dramatically restricted by the inherent shortcomings of fast charge recombination because of incomplete polymerization. Thus, increasing the extent of polymerization can be one of an efficient way to enhance its photocatalytic activity. Herein, a molten salt post-treatment approach has been developed to reconstruct pristine g-C$_3$N$_4$, in which molten salts serve as a generalist for accelerating the polycondensation and deamination reaction. This approach endows g-C$_3$N$_x$ with enriched nitrogen defects, and unique electronic structure, which results in narrower bandgap and higher electrical conductivity, significantly improve visible light harvesting capability and separation efficiency of charge carriers. As a consequence, the g-C$_3$N$_x$ shows 2.2 times higher the H$_2$ evolution rate than bulk g-C$_3$N$_4$. This discovery may open a novel avenue to fabricate highly efficient g-C$_3$N$_4$ catalysts.

## 1. Introduction

Recently, as a metal-free photocatalyst, graphitic carbon nitride (g-C$_3$N$_4$) has attracted intensive attention owing to its potential applications in splitting water [1–4], degrading organic pollutants [5–8] and photosynthesis [9] under visible light. Although g-C$_3$N$_4$ has an excellent visible light response, suitable band position, and chemical stability. However, the pristine g-C$_3$N$_4$ synthesized by thermal polycondensation of nitrogen-rich organic precursors, which still exist a large amount of structural defects including unreacted amino and/or cyano groups due to incomplete polymerization, typically exhibit a lower crystallinity [10]. These structural defects often act as recombination centers for electron-hole pairs during photocatalytic reactions, significantly reducing the charge separation efficiency and thus decreasing the photocatalytic activity. To overcome these problems, great efforts have been made on modification of g-C$_3$N$_4$, such as doping with heteroatoms [11–15], coupling with other semiconductors [16–20], morphology construction [21–25] and dye sensitization [26,27]. As a result of these schemes, the activity of g-C$_3$N$_4$ has been improved a lot. To better take advantage of g-C$_3$N$_4$, it is crucial to explore other strategies to optimize its photoreaction activity further.

As liquid reaction media, molten salt has the strong dissolving capability towards oxygen-contained and heteroatom-contained (S and N species) species, resulting in enhanced migration and reaction capability of such species. The activated reaction capability of S and N species in molten salt were recently illustrated. [28] Molten salts also provide a unique inert atmosphere for the reactions. In general, molten salt can serve as a solvent for the materials synthesis, as a soft template for tailoring micro and mesoporosity of the materials, and as a structure-directing agent in the polycondensation and deamination reaction to obtain graphitic materials [29]. The bulk g-C$_3$N$_4$ that prepared by thermal-induced polymerization typically doesn't wholly aggregated. Numerous amino groups (NH$_x$ groups) exist in the g-C$_3$N$_4$ framework, which hinders the separation of photogenerated charges. Zhang et al. post-calcined the co-condensed urea and oxalamide in molten salts to obtain polymer carbon nitrides with ultra-high photocatalytic hydrogen production activity. [30] Lin et al. synthesized a new heptazine-based crystalline carbon nitride by an ionothermal method with high activity towards photocatalytic hydrogen production [31]. Therefore, we envision that it could be an effective means to improve the extent of polymerization of g-C$_3$N$_4$ with reduced structural defects due to the effect of molten salt in the polycondensation and deamination reaction.

In this work, we developed a facile and reliable strategy to prepare N-deficient g-C$_3$N$_4$ *via* a molten salts post-treatment. Nitrogen defects and the improved extent of polymerization in g-C$_3$N$_4$ play a substantial role in extending the visible-light absorption and enhancing the separation efficiency of photogenerated electron-hole pairs. Due to enhanced visible-light absorption and improved charge carrier separation,

---

the g-$C_3N_x$ samples displayed superior photocatalytic hydrogen performance compared to bulk g-$C_3N_4$ under visible light. This work may provide a fresh scheme to promote the photocatalytic activity of g-$C_3N_4$.

## 2. Experimental section

### 2.1. Chemicals and reagents

Melamine, KCl, LiCl, and triethanolamine (TEOA, analytical reagent (AR) grade) were purchased from Sinopharm Chemical Reagent Co., Ltd. and were used without further purification. All other reagents used in this study were analytically pure and used as received.

### 2.2. Synthesis of bulk g-$C_3N_4$

Bulk g-$C_3N_4$ was prepared by thermal polycondensation of melamine. Typically, melamine (10 g) in an alumina crucible (50 mL) with a cover was heated in air at a ramping rate of $2\,°C\,min^{-1}$ to $550\,°C$ in a muffle furnace for 3 h. After cooling to room temperature naturally, the yellow product was collected and then ground into powder in an agate mortar.

### 2.3. Synthesis of g-$C_3N_x$

The g-$C_3N_x$ was synthesized by a molten salt post-treatment method. A eutectic mixture of KCl and LiCl with the molar ratio of 41:59 had a melting point of about $352\,°C$ and was used as the high-temperature solvent for the reactions. Typically, bulk g-$C_3N_4$ (1 g) was ground with KCl (8.2 g) and LiCl (11.8 g) in an agate mortar. Then, the mixture was heated in air at $550\,°C$ in a muffle furnace for 2 h at a ramping rate of $2\,°C\,min^{-1}$. After cooling to room temperature naturally, the product was boiled and washed with deionized water thoroughly to remove residual salts. The product was collected by pumping filtration, following by drying at $60\,°C$ for 12 h.

### 2.4. Characterization

The X-ray diffraction (XRD) patterns of the as-prepared samples were collected on a powder X-ray diffractometer (Cu Kα radiation source, D8, Bruker). The morphologies of the samples were investigated by a field-emission scanning electron microscopy (FE-SEM, Hitachi S4800). Fourier-transform infrared (FT-IR) spectra were obtained on a Tensor 27 spectrometer (Bruker). The solid-state $^{13}C$ NMR experiments were performed on a Bruker Advance III 500 spectrometer. UV–vis (UV–vis) diffuse reflectance spectra were recorded on a Shimadzu UV-2450 spectrophotometer equipped with an integrating sphere, then converted into absorption spectra by Kubelka-Munk transformation. Photoluminescence (PL) spectra were measured at room temperature using a Fluoromax-4 Spectrophotometer (Horiba Jobin Yvon). The excitation wavelength was 325 nm, and the emission slit was 1.0 nm. Elemental analysis was carried out on a Thermo-Scientific Flash Smart micro-analyzer. The XPS patterns were measured on an electronic energy spectrum (AXIS UltraDLD, Kratos group) at 300 W using Mg Kα X-rays as the excitation source. Steady-state/time-resolved photoluminescence emission spectra (365 nm excitation) were measured at room temperature with a fluorescence spectrophotometer (PTI, DeltaFlex). Electron paramagnetic resonance (EPR) spectra were taken using a Bruker model ER200-SRC spectrometer.

### 2.5. Photocatalytic $H_2$ production

The photocatalytic $H_2$ evolution reactions were carried out in a Pyrex reaction cell connected to a closed gas circulation and evacuation system using a 300 W Xe lamp with a cut-off filter ($\lambda > 420$ nm). 0.2 g of photocatalyst was dispersed in an aqueous solution (100 mL) containing (20 vol. %) triethanolamine (TEOA) as a sacrificial agent by sonication. Before irradiation, the reactor was well-evacuated by a vacuum pump to remove the dissolved air in water. The amount of $H_2$ evolved was analyzed by on-line gas chromatography with TCD detector (Hua'ai, GC9160, China, MS-5 A, argon as carrier gas). The co-catalyst Pt for the promotion of hydrogen evolution was photo-deposited *in situ* on the photocatalyst with $H_2PtCl_6·6H_2O$ as a precursor. The temperature for all photocatalytic reactions was kept at $25\,°C ± 5\,°C$.

### 2.6. Photoelectrochemical measurements

The photoelectrochemical properties of the samples were examined by electrochemical impedance spectroscopy (EIS) and photocurrent response measurements on a PARSTAT 4000 electrochemical workstation using a standard three-electrode cell with a working electrode, a platinum foil counter electrode, and an Ag/AgCl reference electrode. $Na_2SO_4$ (0.1 M) was used as the electrolyte solution. The working electrode was prepared by dip-coating photocatalyst slurry on FTO glass electrode ($1.0 × 1.0$ cm$^2$) and heating it at $60\,°C$ overnight. Mott-Schottky plots were obtained under direct current potential polarization at different frequencies (1.0, 1.2, and 1.5 kHz). For photocurrent measurements, the applied over-potential was set to be 0.5 V (*vs*. Ag/AgCl). Electrochemical impedance spectroscopy (EIS) measurements were carried out with a sinusoidal ac perturbation of 10 mV applied over the frequency range of $0.01–10^5$ Hz.

## 3. Results and discussion

The crystal structures of the bulk g-$C_3N_4$ and g-$C_3N_x$ were demonstrated by their XRD patterns. As shown in Fig. 1, the XRD pattern for the bulk g-$C_3N_4$ displays two distinct diffraction peaks located at 2θ of about 13.0° and 27.4°, corresponding to the (100) and (002) crystal planes of g-$C_3N_4$, which represent the in-plane structural packing motif and the stacking of the conjugated aromatic systems in the layered structure, respectively. [32–34] The XRD patterns of g-$C_3N_x$ were similar to that of bulk g-$C_3N_4$, indicating that the general structure of g-$C_3N_4$ was preserved after flux treatment. However, it is worth noting that the (100) peak decreases, which is ascribed to the decreased planar size of the layers. The (002) peak shifts slightly from 27.4° to 27.6°, suggesting the decrease of interlayer distance in g-$C_3N_x$ [35]. The full width at half maximum (FWHM) of the strongest diffraction peak in g-$C_3N_x$ is significantly narrowed than bulk g-$C_3N_4$, and this observation suggests the improved crystallinity of g-$C_3N_x$. Additionally, both peaks gradually weakened after flux post-treatment, suggesting the loss of ordered structures within the framework, which is in good agreement with the results of SEM and TEM.
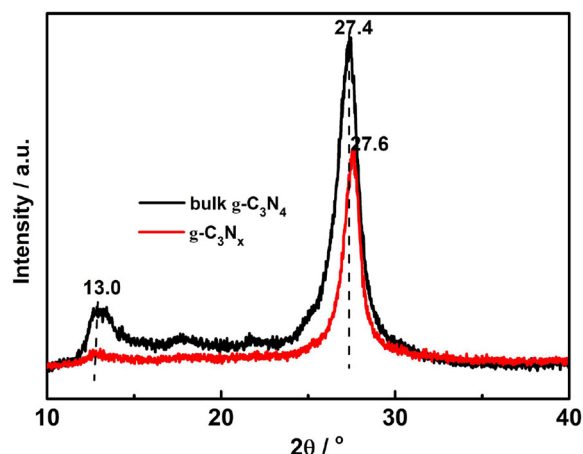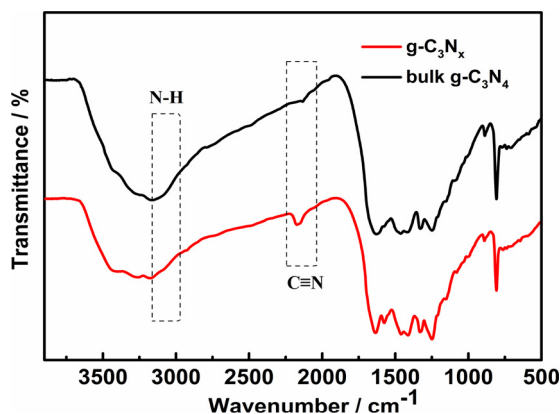


**Fig. 1.** XRD patterns of g-$C_3N_4$ and g-$C_3N_x$.

**Fig. 2.** FTIR spectra of bulk g-C$_3$N$_4$ and g-C$_3$N$_x$.

The morphology of bulk g-C$_3$N$_4$ and g-C$_3$N$_x$ was investigated by SEM and TEM. As shown in Fig.S1, bulk g-C$_3$N$_4$ displays the typical stacked lamellar structure, and the size distribution is uneven (Fig. S1a and S1c). After flux treatment, the plate-like g-C$_3$N$_4$ has been corroded and it appears as irregular structures (Fig. S1b and S1d), probably due to the random oxidation by the flux, which is consistent with the XRD result. The nitrogen adsorption and desorption isotherms measurements were used to examine the effect of flux treatment on the specific surface area and pore structure of samples. The BET specific surface areas (S$_{BET}$) of bulk g-C$_3$N$_4$ and g-C$_3$N$_x$ are 75.85 m$^2$ g$^{-1}$ and 48.35 m$^2$ g$^{-1}$ (Table S1). The BET specific surface area of the g-C$_3$N$_x$ samples decreased, which is also in good agreement with the XRD result.

The FTIR spectra of bulk g-C$_3$N$_4$ and g-C$_3$N$_x$ are shown in Fig. 2. Similar FTIR spectra regarding the typical CN heterocycle skeletal vibration are observed for bulk g-C$_3$N$_4$ and g-C$_3$N$_x$. The peak located at about 810 cm$^{-1}$ is related to the out-of-plane bending mode of tri-s-triazine rings, which indicates the existence of basic melon units with NH/NH$_2$ groups and several strong bands located in the 1200-1600 cm$^{-1}$ range are ascribed to the stretching vibrations of aromatic CN heterocycles. In addition, the broad peak at 2900-3500 cm$^{-1}$ originates from the N−H vibration and the O−H vibration, caused by the surface uncondensed amine groups and the absorbed water molecules. [36,37] However, compared to bulk g-C$_3$N$_4$, it is readily observed that two obvious differences in the FTIR spectra of the g-C$_3$N$_x$ samples. One is a decrease in the intensity of the N−H stretching peaks at 3000-3300 cm$^{-1}$. The other is that a new peak appears at 2172 cm$^{-1}$, corresponding to an asymmetric stretching vibration of cyano groups (−C≡N or N=C=), which is resulted from the loss of NH$_3$ group. [1,34,38–40]

Solid-state $^{13}$C NMR spectra were employed to investigate the chemical state of carbon. As displayed in Fig. S2, The NMR spectra of bulk g-C$_3$N$_4$ and g-C$_3$N$_x$ show two strong peaks at 164.4 and 156.3 ppm corresponding to the chemical shifts of N−C(−NH$_x$)=N and N−C(=N)−N in g-C$_3$N$_4$, respectively, which is in line with the previous reports [1,5,41]. These characteristics indicate the simultaneous presence of the melem and melon structures. The $^{13}$C spectra of bulk g-C$_3$N$_4$ and g-C$_3$N$_x$ look almost the same, meaning that the frameworks were well-preserved after the molten salt post-treatment. The result is in accordance with XRD and FTIR.

To further investigate the elemental chemical state and composition in bulk g-C$_3$N$_4$ and g-C$_3$N$_x$, C 1s and N 1s core levels were investigated by XPS. As shown in Fig. 3a, the main C 1 s spectrum of bulk g-C$_3$N$_4$ can be fitted into three peaks at 290.2, 288.0 and 284.8 eV, respectively. The three peaks are corresponded to the C−O bond, sp$^2$-bonded carbon (N−C = N) and graphitic carbon, respectively. As shown in Fig. 3b, the N 1s spectra of bulk g-C$_3$N$_4$ can be resolved into four different peaks with binding energy at 404.2, 401.0, 399.1, and 398.5 eV, which are attributed to N-oxide or the charging effects in the cyano group, the

bridged or terminal amino groups (NH$_x$ groups), the tertiary nitrogen N-(C)$_3$, and sp$^2$-hybridized nitrogen in a triazine ring (C–N=C), respectively. [1,5,35,42] However, after the flux treatment, apparent changes occur in both C 1s and N 1s XPS spectra of g-C$_3$N$_x$. The 284.2 eV peak related to the C-NH$_x$ bonds can be observed in C 1 s XPS spectra of g-C$_3$N$_x$, which can be taken as additional evidence for the formation of cyano groups since C≡N groups possess similar C1 s binding energies to C-NH$_x$ [33,38,43]. The peak of cyano group is not fitted in N 1 s spectrum due to the overlap of a cyano group and NH$_x$ group. [44] As shown in Table S2, The binding energy of N 1 s (N-(C)$_3$) shifts from 400.1 for bulk g-C$_3$N$_4$ to 399.5 eV for g-C$_3$N$_x$, which can be attributed to the extra electrons redistribution because of the missing nitrogen atoms. [1,5,42] The peak area ratios of the C–N=C to the N-(C)$_3$ peak (N$_{C-N = C}$/N$_{N-(C)3}$) and the N-H$_x$ groups to the N-(C)$_3$ peak (N$_{N-Hx}$/N$_{N-(C)3}$) decreased from 1.37 to 1.07 and 0.59 to 0.24, respectively. This indicates that the loss of N atoms occurs at the C–N=C lattice sites and the uncondensed terminal NH$_x$ species after the flux treatment, not the N-(C)$_3$ lattice sites, which was similar to the result of literature reported previously. [45] An additional K 2p peaks are observed in g-C$_3$N$_x$ (Fig. S3a), which may induce from the surface bonded or layered intercalated K ions. The K ions were mostly likely acted as the charge compensator due to the loss of hydrogen in the form of NH$_3$ during the flux treatment. In addition, the incorporated of K$^+$ in CN framework may increase the conductivity, which would be favorable for the carrier transfer. [13] To further investigate the bulk and surface elemental composition of bulk g-C$_3$N$_4$ and g-C$_3$N$_x$, organic elemental analysis (OEA) measurement was performed. As shown in Table 1, the N/C atomic ratios for bulk g-C$_3$N$_4$ obtained from OEA and XPS were 1.81 and 0.99, respectively. But the N/C atomic ratio decreases to 1.75 and 0.93 for g-C$_3$N$_x$, which indicates the nitrogen defects appear in the g-C$_3$N$_x$ sample. Similar results can also be proved by the results of the EPR spectrum. Nitrogen defects could be generated on g-C$_3$N$_x$ due to the deficiency of NH$_x$ species, which has been confirmed by XPS and XRD. [35] Similar results were also reported by Yu et.al [33]. Based on the above results, simplified reaction scheme of the compound synthesized in this work was shown in Fig. S3b.

Room-temperature EPR analysis was carried out to investigate the electronic band structure of as-prepared samples. Various behaviors of native defects, such as nitrogen or oxygen vacancies, can be evaluated by the EPR. As shown in Fig. 4, the EPR spectrum of g-C$_3$N$_x$ displays a strong symmetrical signal centering at a g factor of 2.003, indicating the generation of unpaired electrons on the carbon atoms of the aromatic ring within π-bonded nanosized clusters and nitrogen vacancies. [46,47] Note that a weak analogous signal is also detected for g-C$_3$N$_4$. This is possible since the thermal polymerization of g-C$_3$N$_4$ may contribute to generating partial disorders (nitrogen defects) in the heat-treatment process, in accordance with the literature. [35]

UV-vis diffuse reflectance spectra of bulk g-C$_3$N$_4$ and g-C$_3$N$_x$ were shown in Fig. 5. The UV–vis adsorption of g-C$_3$N$_x$ has a red shift relative to that of bulk g-C$_3$N$_4$ and g-C$_3$N$_x$ also exhibits stronger light absorption compared to g-C$_3$N$_4$ below the wavelength of 600 nm. The stronger absorption corresponds to its darker color (Fig. 5, inset), and the dark color indicates the existing defects in the g-C$_3$N$_x$. Further analysis using the transformed Kubelka-Munk function by the energy of the light absorption edges shows that the intrinsic absorption edge decreases from 2.76 eV for g-C$_3$N$_4$ to 2.64 eV for g-C$_3$N$_x$ (Fig. 5, inset), which is attributed to the nitrogen vacancies in g-C$_3$N$_x$ [34,47]. Therefore, g-C$_3$N$_x$ has a higher efficiency with regard to visible light absorption and thus may have higher photocatalytic activity than g-C$_3$N$_4$.

To further investigate the effect of the nitrogen defects on the electronic structure of g-C$_3$N$_x$, valence band (VB) XPS was employed to determine the relative positions of its valence band maximum (VBM) and conduction band minimum (CBM). As shown in Fig. 6a, the VB maximum was similar for both bulk g-C$_3$N$_4$ and g-C$_3$N$_x$ (ca. 1.96 eV), which is the contact potential difference between the samples and the analyzer. The VBM of bulk g-C$_3$N$_4$ and g-C$_3$N$_x$ thus is estimated to be
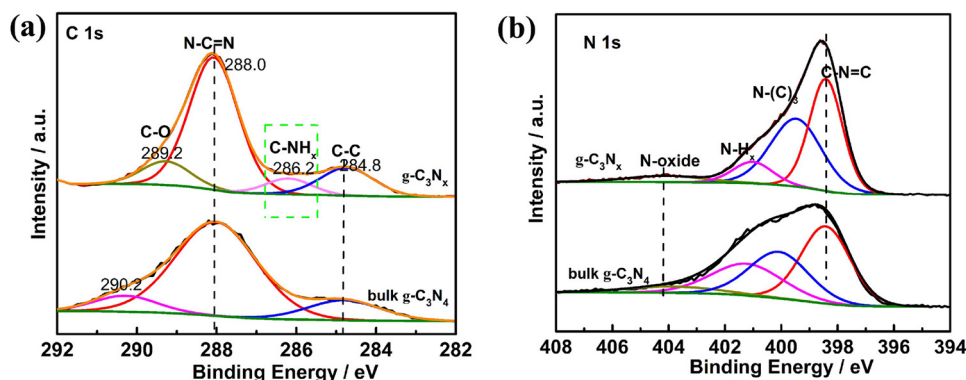
**Fig. 3.** XPS spectra of bulk g-C$_3$N$_4$ and g-C$_3$N$_x$, (a) C 1 s and (b) N 1 s.

**Table 1**
Different atom contents derived from XPS and EA.

| Method | XPS | | | EA | | |
|---|---|---|---|---|---|---|
| Sample | N% | C% | N/C | N% | C% | N/C |
| Bulk g-C$_3$N$_4$ | 48.53 | 48.80 | 0.99 | 61.09 | 33.58 | 1.81 |
| g-C$_3$N$_x$ | 46.07 | 49.13 | 0.93 | 56.27 | 32.04 | 1.75 |
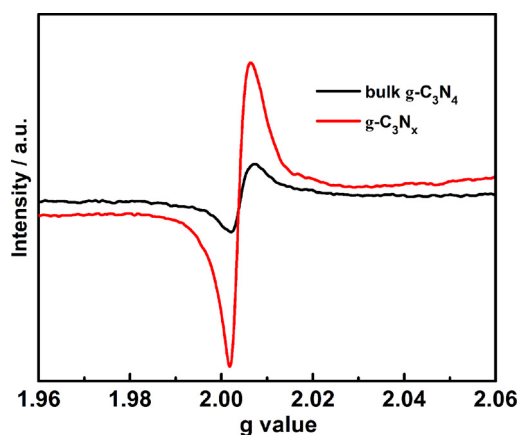


**Fig. 4.** EPR spectra of bulk g-C$_3$N$_4$ and g-C$_3$N$_x$ recorded at room temperature without illumination.
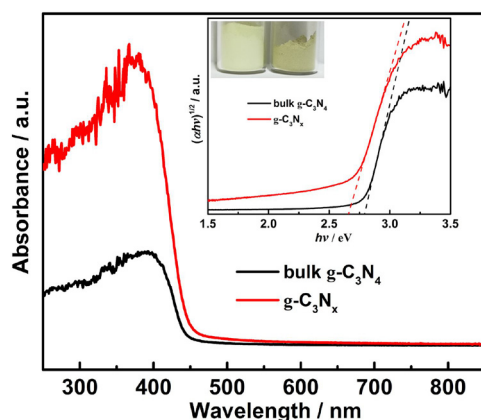


**Fig. 5.** UV–vis diffuse reflectance spectroscopy for bulk g-C$_3$N$_4$ and g-C$_3$N$_x$. The inset shows the bandgap determination form the Tauc plots.

1.52 V *versus* normal hydrogen electrode (NHE) at pH = 7.0 using the formula $E_{NHE}/V = \Phi + 1.96\,eV–4.44\,eV$ ($E_{NHE}$: normal hydrogen electrode, $\Phi$ of 4.00 eV: the electron work function of the analyzer). [33,48]

The data suggest that the VB position was unaffected by the introduction of nitrogen defects into g-C$_3$N$_4$. Therefore, combined with the UV–vis DRS results above, the narrower bandgap of the g-C$_3$N$_x$ sample must originate from a decrease in the CBM position compared to that of g-C$_3$N$_4$ and the optical the CBM potential of g-C$_3$N$_x$ decreases from -1.24 to -1.12 V, which may be due to that the removal of amino groups from g-C$_3$N$_4$ would leave and redistribute extra electrons to their nearest carbon atoms in the g-C$_3$N$_x$ matrix, resulting in the formation of nitrogen vacancy-related states below the CBM of g-C$_3$N$_4$ [34,35]. Based on the above data and combined with the bandgap energies, the band alignments of bulk g-C$_3$N$_4$ and g-C$_3$N$_x$ were shown in Fig. 6b. The Mott-Schottky analysis was used to determine the flat-band potential ($E_{fb}$) of samples. As shown in Fig. S3a and S3b, $E_{fb}$ can be estimated from the intercept on the x-axis by extrapolating the Mott-Schottky plot. The Mott-Schottky plots of all samples under various frequencies exhibit the positive slope in the linear region, indicating they are n-type semiconductors. In this case, the flat-band position of bulk g-C$_3$N$_4$ and g-C$_3$N$_x$ are estimated to be at *ca.* -1.87 V and *ca.* -1.78 V *vs.* Ag/AgCl at pH = 7.0, which correspond to *ca.* -1.25 V and *ca.* -1.16 V *vs.* Normal hydrogen electrode (NHE) at pH = 7.0, respectively, indicating all of the samples thermodynamically enable photocatalytic reduction of water ($2H^+ + 2e^- = H_2$, $E_0 = -0.41$ V *vs.* NHE at pH = 7.0). The results of the Mott-Schottky plots further confirm the CBM of the g-C$_3$N$_x$ sample decrease due to the nitrogen defects, as shown in Fig. S4a and S4b.

Photoluminescence spectroscopy is one of the most powerful techniques for characterizing the recombination of photogenerated charge carriers. Fig. 7a shows the PL spectra of bulk g-C$_3$N$_4$ and g-C$_3$N$_x$ excited at 325 nm at room temperature. Bulk g-C$_3$N$_4$ shows a stronger PL emission peak than that of g-C$_3$N$_x$, which indicates the quick recombination of photogenerated electron-hole pairs on the surface. However, obvious fluorescence quenching is observed for g-C$_3$N$_x$. A lower peak intensity of g-C$_3$N$_x$ signals a lower recombination rate of photogenerated electron-hole pairs relative to bulk g-C$_3$N$_4$. It seems that the formation of nitrogen vacancies is beneficial to the charge separation on the g-C$_3$N$_x$ photocatalyst since the surface nitrogen-deficient sites possess extra electrons and tend to trap photogenerated holes, contributing to the reducing spatial overlap between photogenerated carriers. [35,47] Time-resolved photoluminescence spectra of bulk g-C$_3$N$_4$ and g-C$_3$N$_x$ were obtained (Fig. 7b). The acquired PL lifetimes for bulk g-C$_3$N$_4$ and g-C$_3$N$_x$ were 3.00 and 2.13 ns, respectively. The lower lifetime implies the efficient charge separation and transfer occurring in g-C$_3$N$_x$.

Photoelectrochemical measurements have been conducted to investigate the charge transport property of bulk g-C$_3$N$_4$ and g-C$_3$N$_x$. As shown in Fig.8a, the g-C$_3$N$_x$ sample exhibits higher photocurrent density than bulk g-C$_3$N$_4$ owing to its lower recombination of photogenerated carriers. The photocurrent density verifies the results of PL. Fig. 8b displays the EIS plots of bulk g-C$_3$N$_4$ and g-C$_3$N$_x$ in the dark.
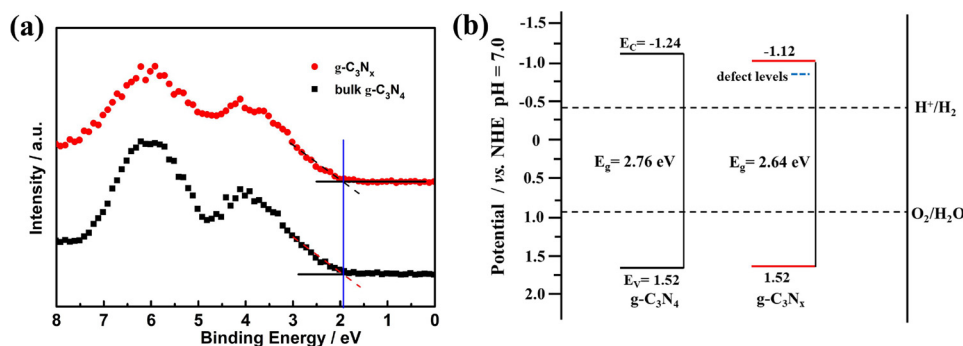
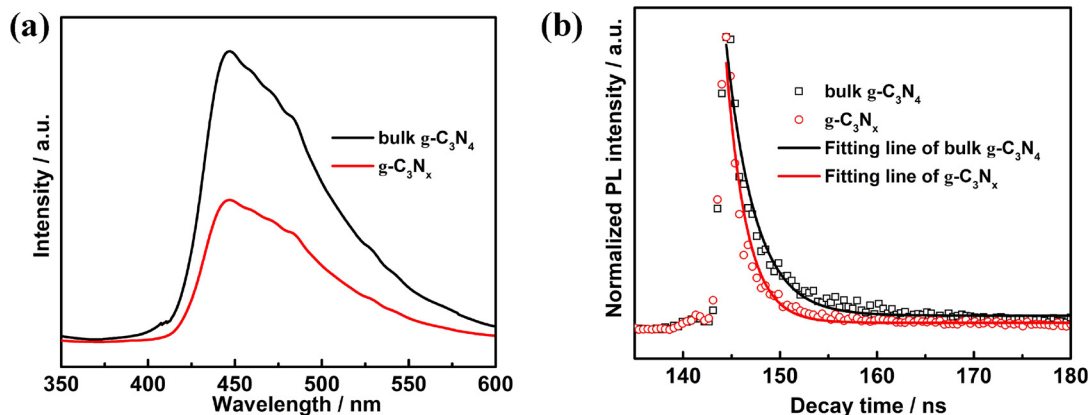**Fig. 6.** (a) High-resolution valence band XPS spectra, (b) schematic illustration of the band structure.



**Fig. 7.** (a) PL spectra of bulk g-$C_3N_4$ and g-$C_3N_x$ (325 nm excitation) and (b) Time-resolved PL spectra of bulk g-$C_3N_4$ and g-$C_3N_x$.



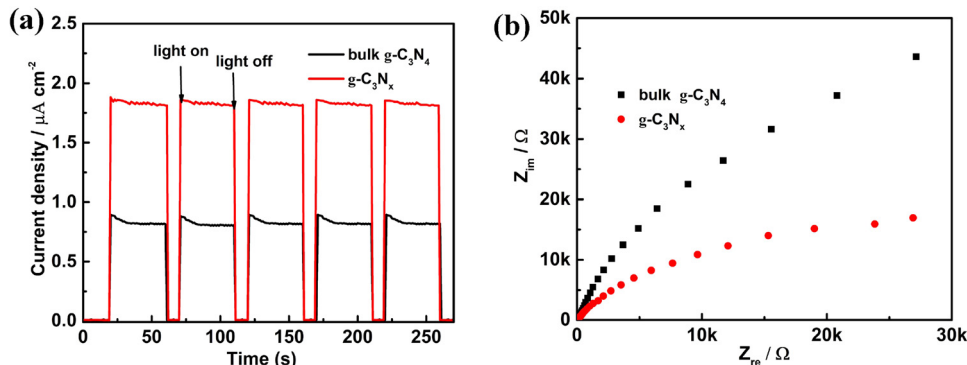**Fig. 8.** (a) Periodic on-off photocurrent response under visible light irradiation and (b) electrochemical impedance spectroscopy plots of bulk g-$C_3N_4$ and g-$C_3N_x$ in the dark.

Obviously, the g-$C_3N_x$ sample has smaller arc radius in compared with bulk g-$C_3N_4$, suggesting much lower electron-transfer resistance than bulk g-$C_3N_4$, and therefore, defines higher charge transfer efficiency.

The photocatalytic $H_2$ evolution over bulk g-$C_3N_4$ and g-$C_3N_x$ is shown in Fig. 9. The $H_2$ evolution rate over bulk g-$C_3N_4$ is 190.2 μmol h$^{-1}$, while it is 403.1 μmol h$^{-1}$ over g-$C_3N_x$. The latter is about 2.2 times of the former. It reveals that the nitrogen defects in g-$C_3N_x$ promote the photocatalytic performance greatly. As it is known, the photocatalytic reaction is affected strongly by the electronic structure of the semiconductive photocatalyst. It is clear that the nitrogen defects in g-$C_3N_x$ would change the electronic structure of g-$C_3N_4$, consequently resulting in enhancing efficient separation of photo-generated charge carriers and extending spectral response range, which is a benefit to the improvement of photocatalytic activity under visible light.

The stability and recyclability of g-$C_3N_x$ were also studied. As shown

in Fig. 10, g-$C_3N_x$ shows nearly no obvious decrease in the $H_2$ evolution activity, exhibiting high stability in photocatalytic performance during three reaction cycles. The results indicate that the nitrogen-deficient g-$C_3N_x$ sample has sufficient stability for the photocatalytic water splitting, which is significant for its practical applications.

## 4. Conclusions

In summary, N-deficient g-$C_3N_4$ were successfully prepared *via* a molten salt post-treatment method. Compared with bulk g-$C_3N_4$, the obtained g-$C_3N_x$ product had a slightly narrowed bandgap and extended visible light absorbance due to the nitrogen defects in the band gap. Meanwhile, it exhibits an enhanced charge separation and transfer efficiency. Consequently, the g-$C_3N_x$ sample displays a stable photocatalytic $H_2$ evolution rate up to 403.1 μmol h$^{-1}$, which is about 2.2 times of that on bulk g-$C_3N_4$, which can be ascribed to the synergistic

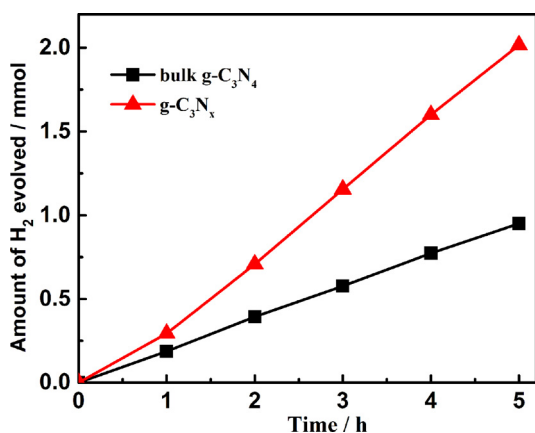**Fig. 9.** Time courses of photocatalytic hydrogen evolution of bulk g-$C_3N_4$ and g-$C_3N_x$.
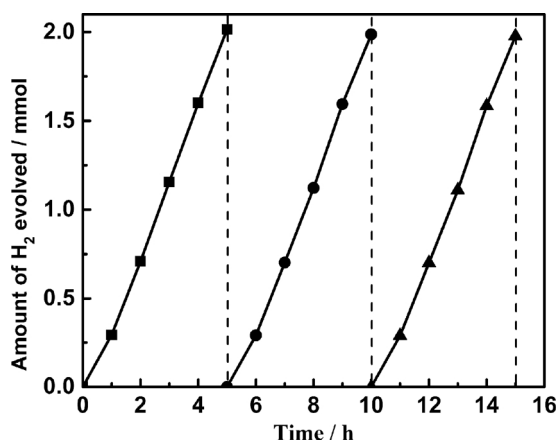


**Fig. 10.** Stability test of hydrogen evolution for g-$C_3N_x$ under visible light irradiation.

effect of the improved extent of polymerization with low structural defects, the decreased band gap, and the efficient separation of charge carriers. This study provides a new strategy to develop nitrogen deficient g-$C_3N_4$ with high photocatalytic activity for hydrogen generation.

## Appendix A. Supplementary data

Supplementary material related to this article can be found, in the online version, at doi:https://doi.org/10.1016/j.apcatb.2018.07.021.

## References

[1] Y. Chen, X. Wang, J. Phys. Chem. C 122 (2018) 3786–3793.
[2] Z. Sun, M. Zhu, M. Fujitsuka, A. Wang, C. Shi, T. Majima, ACS Appl. Mater. Inter. 9 (2017) 30583–30590.
[3] H. Bian, Y. Ji, Y. Yan, P. Li, L. Li, Y. Li, S. Frank Liu, Small 14 (2018) 1703003–1703012.
[4] W. Wang, T. An, G. Li, D. Xia, H. Zhao, J.C. Yu, P.K. Wong, Appl. Catal. B-Environ. 217 (2017) 570–580.
[5] Y. Cui, Z. Ding, X. Fu, X. Wang, Angew. Chem. Int. Edit 51 (2012) 11814–11818.
[6] X. Wang, M. Hong, F. Zhang, Z. Zhuang, Y. Yu, ACS Sustain. Chem. Eng. 4 (2016) 4055–4063.
[7] Y. Hou, Z. Wen, S. Cui, X. Guo, J. Chen, Adv. Mater. 25 (2013) 6291–6297.
[8] G. Li, X. Nie, Y. Gao, T. An, Appl. Catal. B-Environ. 180 (2016) 726–732.
[9] N. Sagara, S. Kamimura, T. Tsubota, T. Ohno, Appl. Catal. B-Environ. 192 (2016) 193–198.
[10] L. Lin, H. Ou, Y. Zhang, X. Wang, ACS Catal. 6 (2016) 3921–3931.
[11] J.-W. Zhang, S. Gong, N. Mahmood, L. Pan, X. Zhang, J.-J. Zou, Appl. Catal. B-Environ. 221 (2018) 9–16.
[12] X. Sun, D. Jiang, L. Zhang, W. Wang, Appl. Catal. B-Environ. 220 (2018) 553–560.
[13] M. Zhang, X. Bai, D. Liu, J. Wang, Y. Zhu, Appl. Catal. B-Environ. 164 (2015) 77–81.
[14] J. Fu, B. Zhu, C. Jiang, B. Cheng, W. You, J. Yu, Small 13 (2017) 1603938–1603947.
[15] Z.-F. Huang, J. Song, L. Pan, Z. Wang, X. Zhang, J.-J. Zou, W. Mi, X. Zhang, L. Wang, Nano Energy 12 (2015) 646–656.
[16] Y. Wang, Y. Wang, X. Chen, J. Wang, Y. Zhu, Appl. Catal. B-Environ. 220 (2018) 337–347.
[17] H. Xu, J. Yi, X. She, Q. Liu, L. Song, S. Chen, Y. Yang, Y. Song, R. Vajtai, J. Lou, H. Li, S. Yuan, J. Wu, P.M. Ajayan, Appl. Catal. B-Environ. 220 (2018) 379–385.
[18] M. Zhu, S. Kim, L. Mao, M. Fujitsuka, J. Zhang, X. Wang, T. Majima, J. Am. Chem. Soc. 139 (2017) 13234–13242.
[19] L. Yao, D. Wei, Y. Ni, D. Yan, C. Hu, Nano Energy 26 (2016) 248–256.
[20] G. Li, X. Nie, J. Chen, Q. Jiang, T. An, P.K. Wong, H. Zhang, H. Zhao, H. Yamashita, Water Res. 86 (2015) 17–24.
[21] Q. Liang, Z. Li, X. Yu, Z.-H. Huang, F. Kang, Q.-H. Yang, Adv. Mater. 27 (2015) 4634–4639.
[22] D.J. Martin, K. Qiu, S.A. Shevlin, A.D. Handoko, X. Chen, Z. Guo, J. Tang, Angew. Chem. Int. Edit. 53 (2014) 9240–9245.
[23] L. Zhang, Q. Liu, Y. Chai, W.-L. Dai, Int. J. Hydrogen Energy 43 (2018) 5591–5602.
[24] N. Tian, Y. Zhang, X. Li, K. Xiao, X. Du, F. Dong, G.I.N. Waterhouse, T. Zhang, H. Huang, Nano Energy 38 (2017) 72–81.
[25] C. Liu, H. Huang, L. Ye, S. Yu, N. Tian, X. Du, T. Zhang, Y. Zhang, Nano Energy 41 (2017) 738–748.
[26] J. Xu, Y.L. Li, S. Peng, G. Lu, S. Li, Phys. Chem. Chem. Phys. 15 (2013) 7657–7665.
[27] K. Takanabe, K. Kamata, X. Wang, M. Antonietti, J. Kubota, K. Domen, Phys. Chem. Chem. Phys. 12 (2010) 13020–13025.
[28] X. Liu, N. Fechler, M. Antonietti, Chem. Soc. Rev. 42 (2013) 8237–8265.
[29] J. Zhao, L. Ma, H. Wang, Y. Zhao, J. Zhang, S. Hu, Appl. Surf. Sci. 332 (2015) 625–630.
[30] G. Zhang, G. Li, Z.A. Lan, L. Lin, A. Savateev, T. Heil, S. Zafeiratos, X. Wang, M. Antonietti, Angew. Chem. Int. Edit. 56 (2017) 13445–13449.
[31] L. Lin, W. Ren, C. Wang, A.M. Asiri, J. Zhang, X. Wang, Appl. Catal. B-Environ. 231 (2018) 234–241.
[32] P. Qiu, C. Xu, H. Chen, F. Jiang, X. Wang, R. Lu, X. Zhang, Appl. Catal. B-Environ. 206 (2017) 319–327.
[33] H. Yu, R. Shi, Y. Zhao, T. Bian, Y. Zhao, C. Zhou, G.I.N. Waterhouse, L.Z. Wu, C.H. Tung, T. Zhang, Adv. Mater. 29 (2017) 1605148–1605155.
[34] P. Niu, G. Liu, H.-M. Cheng, J. Phys. Chem. C 116 (2012) 11013–11018.
[35] Z. Hong, B. Shen, Y. Chen, B. Lin, B. Gao, J. Mater. Chem. A 1 (2013) 11754–11761.
[36] Y. Guo, Q. Liu, Z. Li, Z. Zhang, X. Fang, Appl. Catal. B-Environ. 221 (2018) 362–370.
[37] W. Fang, J. Liu, L. Yu, Z. Jiang, W. Shangguan, Appl. Catal. B-Environ. 209 (2017) 631–636.
[38] H. Gao, S. Yan, J. Wang, Y.A. Huang, P. Wang, Z. Li, Z. Zou, Phys. Chem. Chem. Phys. 15 (2013) 18077–18084.
[39] Y. Wang, Y. Li, W. Ju, J. Wang, H. Yao, L. Zhang, J. Wang, Z. Li, Carbon 102 (2016) 477–486.
[40] W. Lei, D. Portehault, R. Dimova, M. Antonietti, J. Am. Chem. Soc. 133 (2011) 7121–7127.
[41] B.V. Lotsch, M. Doblinger, J. Sehnert, L. Seyfarth, J. Senker, O. Oeckler, W. Schnick, Chem.-Euro. J. 13 (2007) 4969–4980.
[42] S. Thaweesak, S. Wang, M. Lyu, M. Xiao, P. Peerakiatkhajohn, L. Wang, Dalton Trans. 46 (2017) 10714–10720.
[43] D. Zhang, Y. Guo, Z. Zhao, Appl. Catal. B-Environ. 226 (2018) 1–9.
[44] V.N. Khabashesku, J.L. Zimmerman, J.L. Margrave, Chem. Mater. 12 (2000) 3264–3270.
[45] J. Ding, W. Xu, H. Wan, D. Yuan, C. Chen, L. Wang, G. Guan, W.-L. Dai, Appl. Catal. B-Environ. 221 (2018) 626–634.
[46] Y. Cui, G. Zhang, Z. Lin, X. Wang, Appl. Catal. B-Environ. 181 (2016) 413–419.
[47] C.Q. Xu, K. Li, W.D. Zhang, J. Colloid Interf. Sci. 495 (2017) 27–36.
[48] S. Yang, Y. Gong, J. Zhang, L. Zhan, L. Ma, Z. Fang, R. Vajtai, X. Wang, P.M. Ajayan, Adv. Mater. 25 (2013) 2452–2456.